Corrosion resistance of amorphous carbon film in 3.5 wt% NaCl solution for marine application

Jing Wei [a, b], Peng Guo [a], Linlin Liu [a], Hanchao Li [a, c], Hao Li [a], Shuyuan Wang [a, b], Peiling Ke [a, b], Hidetoshi Saito [a, d], Aiying Wang [a, b, *]

[a] Key Laboratory of Marine Materials and Related Technologies, Zhejiang Key Laboratory of Marine Materials and Protective Technologies, Ningbo Institute of Materials Technology and Engineering, Chinese Academy of Sciences, Ningbo, 315201, China
[b] Center of Materials Science and Optoelectronics Engineering, University of Chinese Academy of Sciences, Beijing, 100049, China
[c] School of Physical Science and Technology, Shanghai Tech University, Shanghai, 201210, China
[d] Graduate School of Engineering, Nagaoka University of Technology, 940-2188, Nagaoka, Japan

ARTICLE INFO

ABSTRACT

In this work, we fabricated the tetrahedral amorphous carbon (ta-C) films with thicknesses of 20 nm, 40 nm and hydrogenated diamond-like carbon (DLC:H) film with thickness of 1.1 μm on 316 stainless steel substrate (316SS). The electrochemical corrosion performances of two typical amorphous carbon (a-C) films in 3.5 wt% NaCl solution were focused. Results revealed that both ultrathin ta-C films exhibited superior corrosion resistance than that of DLC:H film, because the high content of sp^3 bonded carbon and low porosity in ta-C films significantly suppressed the diffusion of corrosion media. However, a thickness threshold beyond 20 nm was proposed to obtain the superior corrosion resistance for ta-C films due to the emerged pitting of 316SS. For DLC:H film, the deterioration of corrosion resistance could be attributed to the hydrogen-containing interface, the large sp^2 clusters with high electron transport, and the higher porosity density in carbon matrix.

© 2020 Elsevier Ltd. All rights reserved.

1. Introduction

Amorphous carbon (a-C) films stand out from various surface protective coatings due to their excellent mechanical properties, low friction coefficient, high wear resistance and good chemical inertness [1−3]. In addition to suffering from mechanical wear, a-C films are also invaded by corrosive media in practical applications, such as body fluids from the biomedical area, seawater from marine environment, cutting fluid from cutting field, etc [4−9]. Under complex working conditions, the existence of corrosive media may accelerate mechanical wear and trigger fatal damage of protective coatings or components, revealing the great significance to study the electrochemical corrosion properties [10,11].

Normally, a-C films act as good physical barrier due to their amorphous structure and excellent chemical inertness. The

physical, chemical and electrochemical properties of a-C films can be readily tuned by the sp^2/sp^3 bonding ratio, the organization of sp^2 clusters, hydrogen content and element doping, which in return depend on the deposition methods and the types of a-C film [12,13]. Film thickness, atomic bonds and porosity of a-C film have been reported to be the main factors determining its electrochemical corrosion performance. The thickness of a-C film affects the corrosion barrier effect. In general, an increase in thickness results in an enhanced barrier effect [14]. Moreover, the sp^2/sp^3 ratio of a-C film could also determine its electrochemical properties [15,16]. The crosslinking structure with high sp^3 bonded carbon content contributes to the improved chemical stability and suppressed electron transportation, which finally promotes the corrosion resistance. More importantly, the penetrated defects in a-C film play a decisive role in triggering the occurrence of corrosion [17−19].

As two typical a-C films, hydrogen-containing diamond-like carbon (DLC:H) and hydrogen-free tetrahedral amorphous carbon (ta-C) film have gained increasing attention as effective corrosion protection coatings for metal substrate [20,21]. For DLC:H with relative low sp^3 content, they can exhibit good protective

performance at a relative larger thickness. Y. UEMATSU et al. [14] pointed out that DLC:H with thickness of 12 μm effectively improved the corrosion fatigue strength of magnesium alloy in demineralised water. Huang et al. [22] also verified the good corrosion protection of steel substrate provided by 1.7 μm thick DLC:H in various solutions. For ta-C film, characterized by high sp^3 content and ultra-smooth surface, is able to realize uniform coverage at nanometer scale, showing great potential in the field of ultra-thin protective coatings. Zhong et al. [23] and Tan et al. [24] found that ta-C film with a thickness of ~2 nm was effective to protect the magnetic storage medium against corrosion in de-ionized water and oxalic acid solution. Apparently, both the two typical a-C film could find its use in diverse corrosive environments. Although some works have reported the specific electrochemical behavior for a certain type of a-C, the dependence of electrochemical properties upon different kinds of a-C is still not understood clearly. Meanwhile, the underlining corrosion mechanism of a-C film in terms of thickness, atomic bonds and porosity has been little clarified. Considering the typical characteristics for various a-C films, the superimposed effects of thickness, atomic bonds and porosity on their electrochemical corrosion performance could provide theoretical understanding for the application of a-C films used in harsh corrosion environment. Therefore, it is of great significance to investigate the combined influences of thickness, atomic bonds and porosity on the anti-corrosion behaviors of a-C films.

In the present work, DLC:H film by ion beam deposition system and ta-C film by cathodic vacuum arc system were deposited on 316 stainless steel (316SS), the comparative study of their electrochemical corrosion performance was conducted in 3.5 wt% NaCl aqueous solution. The effect of thickness, sp^2/sp^3 ratio and microporosity on corrosion properties of different types of a-C films was investigated, and corrosion mechanism of a-C film was discussed.

2. Experimental procedures

2.1. Deposition of the a-C films

ta-C films with thickness of about 20 nm and 40 nm, which labeled as T-1 and T-2 film, were deposited on P-type silicon (100) wafers and 316SS using a self-built 45° double-bent filtered cathodic vacuum arc (FCVA) system [25]. To clean the substrate and improve the adhesion strength, an arc plasma etching procedure was undertaken first. Subsequently, the ta-C film deposition was proceeded. The duct voltage was 20 V and the arc current was set as 60 A. Substrate bias voltage of −50 V was selected to acquire the optimum sp^3 content.

DLC:H film was prepared by ion beam deposition system which equipped with a linear anode-layer ion source (ALIS). More details about this system have been described in Refs. [26]. During deposition, 38 sccm C_2H_2 gas was fed as carbon source, and the working pressure was 2.6×10^{-3} Pa. Bias voltage of −100 V was applied to the substrate. The typical current and power of the ALIS source were 0.2 A and 260 W, respectively. The DLC:H film with thickness of about 1 μm was labeled as D-1 film.

2.2. Characterization

The cross-sectional images were acquired by field emission scanning electron microscope (FE-SEM, Thermo scientific Verios G4 UC, US). The chemical structure was characterized by a confocal micro-Raman spectrometer (Renishaw inVia-reflex, UK) with a wavelength of 532 nm. X-ray photoelectron spectroscopy (XPS, Axis ultradld, Japan) was utilized to characterize the chemical

composition and bonds of the films using monochromatic Al Kα irradiation. The binding energy was calibrated with C 1s peak at 284.6 eV. High-resolution transmission electron microscopy (HRTEM) images were obtained by a Tecnai F20 with a point-to-point resolution of 0.24 nm. The Focused Ion Beam (FIB) (Carl Zeiss, Auriga) was utilized to prepare the TEM specimens. Electron energy loss spectroscopy (EELS) measurements were conducted on a scanning transmission electron microscope (STEM, Tecnai F20, US). The a-C films and the highly oriented pyrolytic graphite for EELS tests were also fabricated by FIB. A thin Pt layer was deposited to protect the specimen surface prior to FIB processing. The C K-edge spectra and zero-loss peak were collected for 0.01 and 0.005 s, respectively. The background of the C K-edge spectra was subtracted by the power-law model, followed by the removal of plural scattering using the Fourier-ratio deconvolution with the corresponding low-loss spectra. The Gaussian fitting was applied to the π* peak and the energy window 290−305 eV was attributed to the σ* state. The sp^2 fraction was obtained by calculating the area ratio of π* state and σ* state of the unknown sample and referenced to the standard highly oriented pyrolytic graphite (HOPG, 100% sp^2-C bonds).

2.3. Electrochemical corrosion measurements

Electrochemical tests were carried out using a ModuLab (Solartron Analytical) electrochemical workstation in 3.5 wt% NaCl solution at room temperature. The bare 316SS substrate and those coated with T-1, T-2 and D-1 film were used as working electrodes. A platinum mesh and a KCl saturated silver/silver chloride (Ag/AgCl) electrode were employed as counter and reference electrode, respectively. The exposed area of the working electrode was controlled at 1.0 cm^2 by an O-ring. The open circuit potential (OCP) was continuously monitored for 1 h to get a steady potential. Electrochemical impedance spectroscopy (EIS) was recorded at the open circuit potential in the frequency range 100 kHz-10 MHz, with a sinusoidal perturbation of 10 mV. The ZSimpWin software was employed to fit the EIS data. Potentiodynamic polarization was conducted at a scanning rate of 0.5 mV/s, and the potential was swept from −0.6 V to 1.5 V. The polarization curves were analyzed by Modulab software to acquire the electrochemical parameters using Tafel extrapolation method. The scanning vibrating electrode technique (SVET) was used to distinguish the local electrochemical reactivity of the T-1, T-2 and D-1 film coated sample. The current density distribution was acquired by a VersaSCAN micro scanning electrochemical workstation (AMETEK, US). The vibration amplitude and frequency of the micro-electrode were 30 μm and 80 Hz, respectively. The scanning was conducted on an area of 4 mm × 4 mm with 21 × 21 points. For the SVET tests, the samples were fixed into an epoxy resin sleeve. Prior to test, the samples were immersed in the 3.5 wt% NaCl solution for 6 h.

3. Results and discussion

3.1. Characteristic of the films

The hydrogen content of the D-1 film was 20.6 at.%, according to our previous elastic recoil detection analysis (ERD), as described in Ref. [27]. T-1 and T-2 film deposited by FCVA were supposed to be hydrogen free.

Fig. 1 shows the typical cross-sectional morphologies of the T-1, T-2 and D-1 film. The thickness of T-1, T-2, D-1 film was about 22 nm, 43 nm, 1100 nm, respectively. The ultra-thin T-1 and T-2 film had a compact structure, and achieved effective coverage of the substrate. The D-1 film exhibited a less dense structure with relative coarse sectional morphology. For all the three samples,
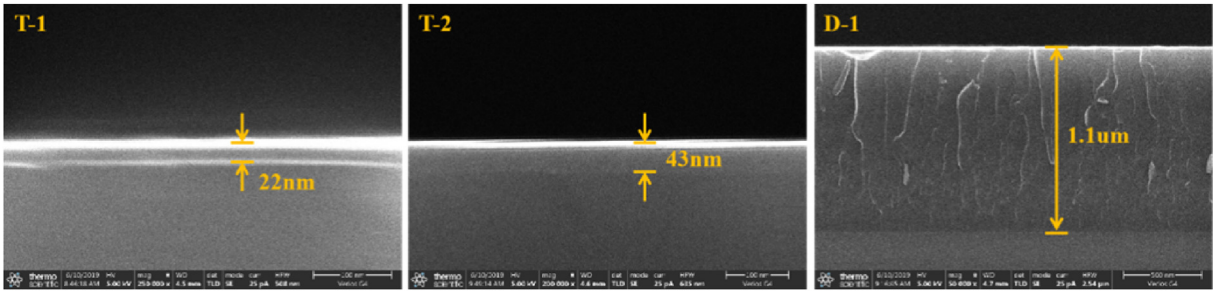
Fig. 1. Cross-sectional morphology of T-1, T-2, D-1 film.

distinguishable interface between the film and the silicon substrate could be observed, and no crack or spalling was observed at the interface, revealing good interfacial bonding.

Raman spectra were employed to characterize the carbon bond structure, as shown in Fig. 2. The Raman spectra were featured by the typical broad peak between 1000 and 1800 cm^{-1}, revealing the typical feature of amorphous carbon. The peak located between 900 and 1000 cm^{-1} was attributed to the second-order peak of silicon substrate, which indicated the good transmittance of T-1 and T-2 films. The spectrum could be fitted with two Gaussian peaks, namely D peak centered at around 1360 cm^{-1} and the G peak at around 1580 cm^{-1}. The integrated area ratios of D peak and G peak of the T-1, T-2, D-1 films, namely I_D/I_G ratios, were 0.58, 0.61, 1.16, respectively. The increased I_D/I_G value is a good indicator of the enhanced sp^2 bonds content and the enlarged sp^2 clusters [28]. Therefore, it could be inferred that the D-1 film possesses higher content of sp^2 bonded carbon than T-1 and T-2 film.

The C1s core level spectra obtained from XPS tests are exhibited in Fig. 3(a). In order to acquire the relative content of sp^2-C and sp^3-C, the C1s spectra were decomposed to three Gaussian peaks at 284.4 eV, 285.2 eV and 286.6 eV that corresponding to sp^2-C, sp^3-C and C$-$O, respectively [29]. Fig. 3(b) showed that the derived sp^3-C
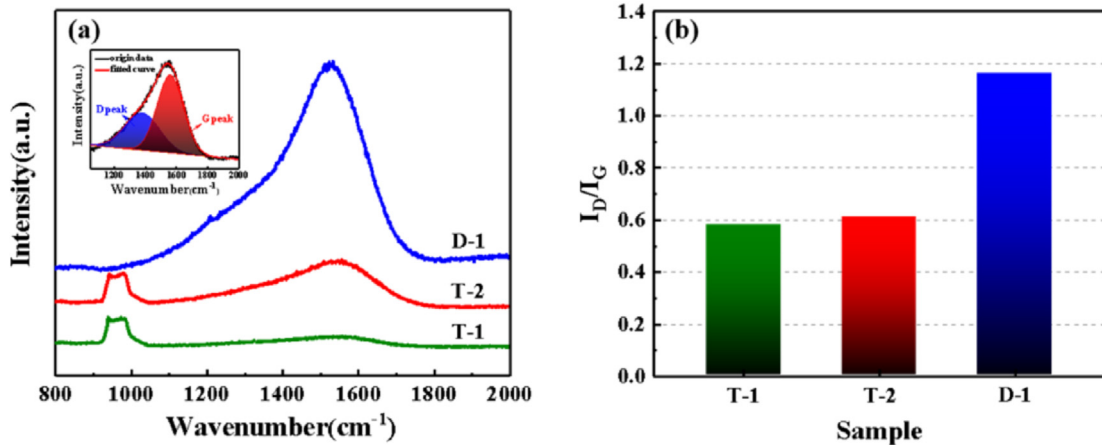

Fig. 2. (a) Raman spectra (Inset shows the fitting details) and (b) I_D/I_G ratio of T-1, T-2, D-1 film.
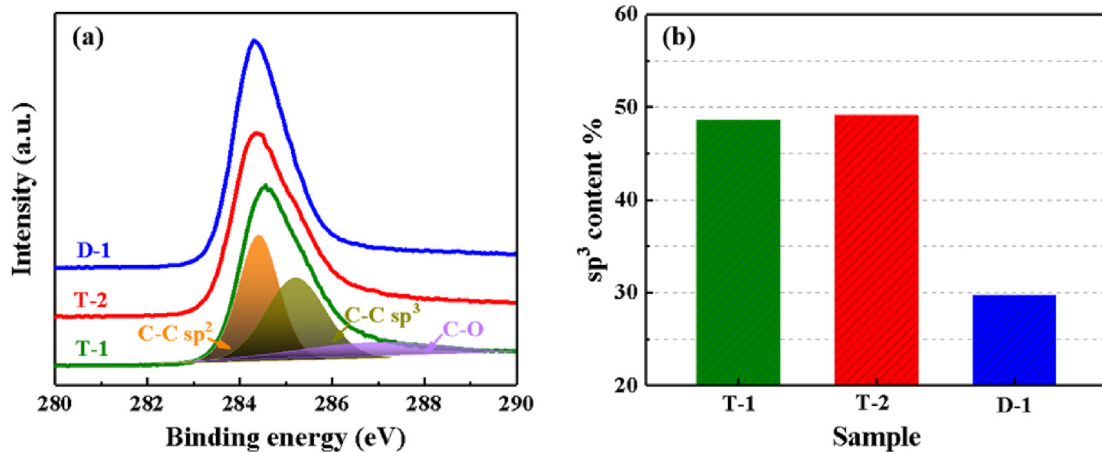

Fig. 3. (a) The XPS C1s core level spectra and (b) sp^3 content of T-1, T-2, D-1 film.

contents of T-1, T-2, D-1 film were 48.6%, 49.1% and 29.7%, respectively, which matched well with the Raman results.

The HRTEM images of the T-1, T-2 and D-1 film are illustrated in Fig. 4. Typical amorphous feature and dense structure were observed in all samples. A clear interface could be identified between the film and Si substrate, based on which the accurate thicknesses of ultra-thin T-1 and T-2 film were confirmed to be 19 nm and 44 nm, respectively.

The cross-sectional STEM images are presented in Fig. 5(a)-(c). In addition to the thick D-1 film, ultra-thin T-1 and T-2 film were capable to achieve the effective coverage of the substrate. Fig. 5(d) shows the carbon K-edge spectra of the films, which consists of a π^*

peak located at about 285 eV stemmed from the sp^2 bonded carbon and a broad absorption edge of σ^* state at 290 eV due to the sp^3 hybridized carbon. The acquired sp^3 bonded carbon contents were summarized in Fig. 5(e). T-1 film had a similar sp^3 bonding fraction with T-2 film (49.5% vs 51.5%), which was much higher than that of D-1 film (31.1%). This was consistent with the Raman and XPS results.

3.2. Electrochemical behaviors

Electrochemical tests were conducted on 316SS substrate and a-C coated 316SS substrate in 3.5 wt% NaCl solution. Fig. 6(a) shows
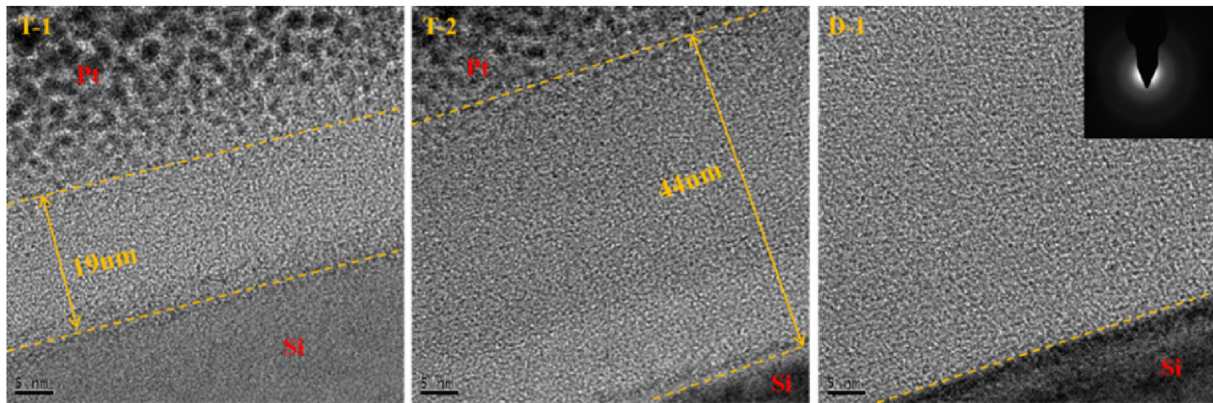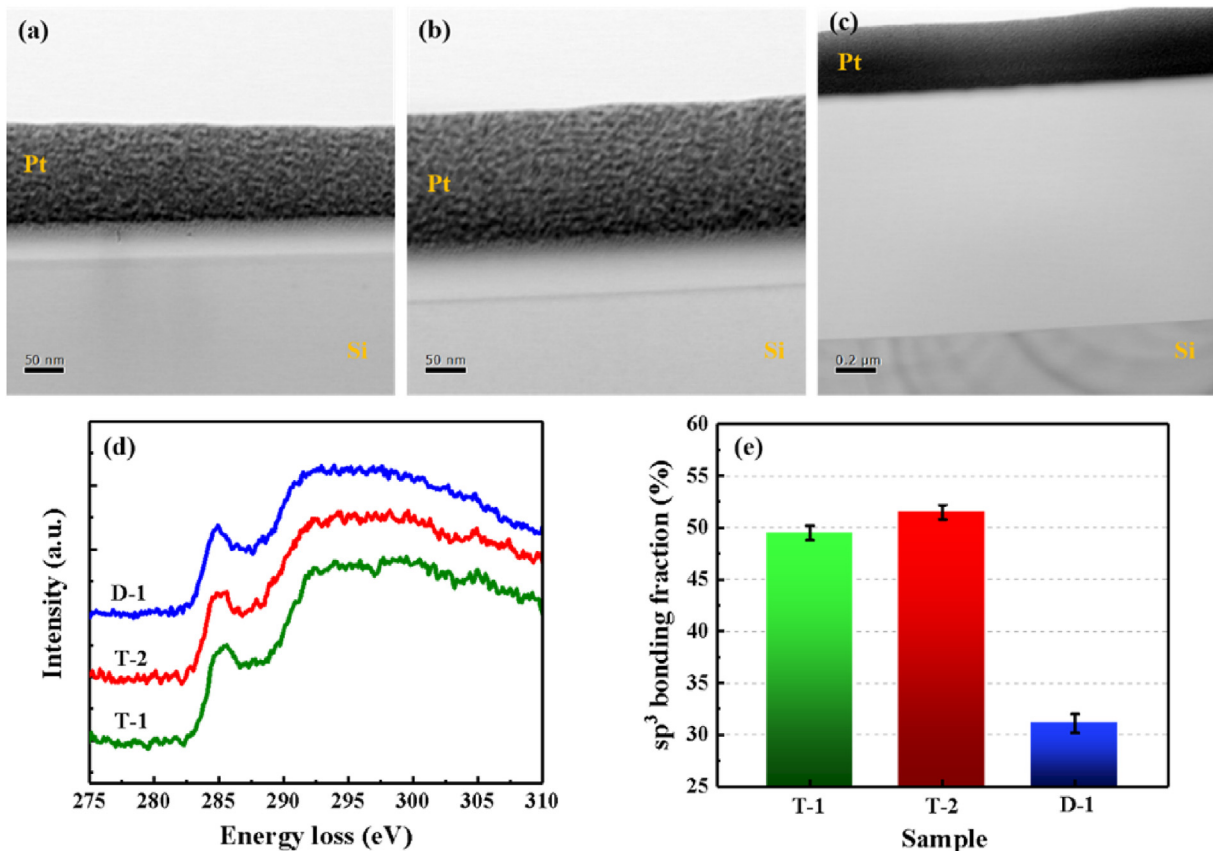

Fig. 4. HRTEM images of T-1, T-2, D-1 film.

Fig. 5. STEM image of (a)T-1, (b)T-2, (c)D-1 film, (d) EELS spectra and (e) derived sp^3 content.
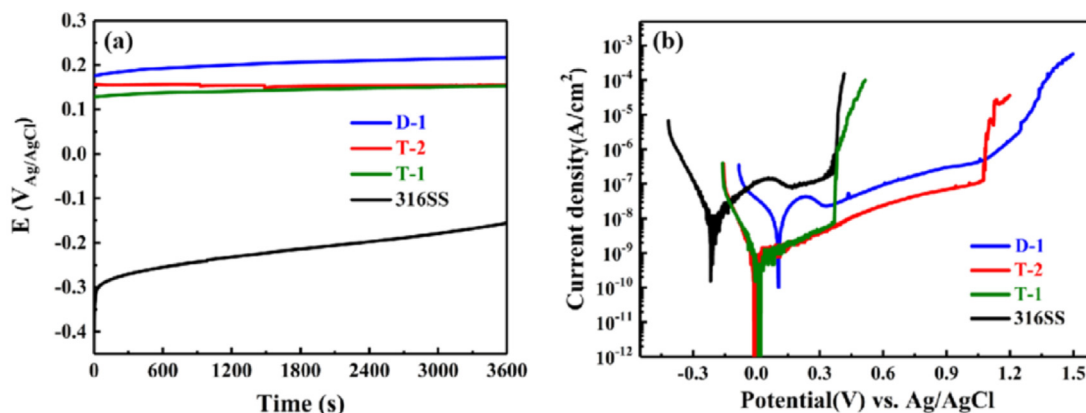
Fig. 6. (a) Open circuit potentials, (b) potentiodynamic polarization curves of T-1, T-2, D-1 film coated 316SS and bare 316SS in 3.5 wt% NaCl solution.

the evolution of open circuit potential (OCP) with test time. Compared with the bare 316SS substrate, the significant increase of OCP values was observed for T-1, T-2, D-1 films coated 316SS, which indicated that the ta-C and DLC:H film significantly enhanced the stability of the substrate. Fig. 6(b) shows the potentiodynamic polarization curves of the samples. Compared with 316SS, the positively shifted corrosion potentials and decreased corrosion current densities of the a-C film coated samples manifested their good corrosion protection effect. It was found that the polarization curve of D-1 film coated 316SS exhibited similar feature as the bare 316SS substrate, while a wide "passive" domain with low current density was observed for D-1 film coated 316SS. The cathodic branch and anodic branch of T-1 film nearly coincided with that of T-2 film except the pitting potential, indicating the same electrode reaction occurred during the electrochemical test. In contrast to T-1 film, T-2 and D-1 films effectively retarded the occurrence of pitting.

Important parameters such as the anodic (β_a) and cathodic (β_b) Tafel slopes, the corrosion current densities (i_{corr}), the corrosion potential (E_{corr}) and the pitting potential (E_{pit}) deduced from Tafel extrapolation method are summarized in Table 1. It could be noted that the β_a of 316SS decreased after coated with a-C films, indicating that the a-C films partially blocked the anode reaction and, thus, retarded the dissolution of 316SS. The observed i_{corr} values were 2.99×10^{-10}, 2.26×10^{-10}, 1.53×10^{-9}, 7.35×10^{-9} A/cm^2 for T-1, T-2, D-1 films coated 316SS and 316SS, respectively. T-1 and T-2 film decreased the corrosion current density of the substrate by an order of magnitude, while only four times reduction was provided by D-1 film. The E_{corr} of T-1, T-2, D-1 films coated sample shifted to more positive value of 0.016, 0.013, 0.095 V vs. Ag/AgCl compared to that of −0.200 V for 316SS, indicating the decreased corrosion tendency. The pitting potential of 316SS substrate was about 0.36 V. With the application of T-2 and D-1 film, the pitting initiation of the substrate was evidently delayed.

EIS tests were conducted to shed more light on the electrochemical corrosion performance and the protection efficiency provided by different a-C films. Fig. 7(a) shows the Bode diagrams.

T-1 and T-2 film coated sample exhibited a capacitive behavior in a wide frequency range from 0.01 Hz to 1000 Hz with phase angle values close to −80° and shifted to ohmic dominated behavior with phase angle reaching 0° at high-frequency range (10−100 kHz). For D-1 coated sample, the phase angle was around −75° in the mid-frequency range (1−10 Hz) and decreased to about 5° at frequency of 1 kHz. Low frequency impedance ($|Z|_{0.01Hz}$) serves as an important index for evaluating corrosion resistance. $|Z|_{0.01Hz}$ of D-1 film coated sample differed a little with the bare 316SS, while T-1 and T-2 film offered 4 times improvement of $|Z|_{0.01Hz}$ value compared to that of D-1 film. The increment of impedance suggested the weakened penetration of aggressive solution into the substrate. Fig. 7(b) shows the Nyquist plots of T-1, T-2, D-1 films coated 316SS and bare 316SS. T-2 film coated sample obtained the largest arc radius, followed by T-1 film coated sample. A significantly decreased arc radius was found for D-1 film coated sample, indicating the reduced corrosion resistance compared to T-1 and T-2 film.

The EIS data were simulated by the equivalent circuits (EC) to understand the physical process occurred in the system. In order to achieve a minimum chi-square value (χ^2) of fitting, two different EC models (Fig. 7(c) and d) were utilized for film coated and uncoated samples. Constant phase elements (CPEs) were used to replace the capacitances in order to achieve accurate fitting of the non-ideal capacitance response. The equivalent circuit consists of the following elements: R_s represents the solution resistance of the electrolyte, and Q_f is related to the capacitance of the film. R_{pore} corresponds to pore resistance originating from the micro-pores defects in the coating. Q_{dl} and R_{ct} are the double layer capacitance and the charge transfer resistance of the interface between substrate and coating. The circuit parameters obtained from the fitting circuits are listed in Table 2.

Regardless of the same test parameters, the different R_s values were observed, which could be attributed to the altered interfacial contact resistances between the electrode and the electrolyte [30,31]. It could be noted that for T-1 and T-2 coated sample, the high n_{dl} values of 0.96 and 0.95 revealed strong capacitive response at the film/substrate interface. Moreover, high R_{ct} value implied that the electrochemical reaction at the interface proceeded at a low speed, which could be attributed to the good insulating property of T-1 and T-2 film. However, adding D-1 film provided little improvement of R_{ct} value compared to that of 316SS substrate. The polarization resistance R_p ($R_p = R_{pore} + R_{ct}$) is an important parameter for evaluating the corrosion resistance. The R_p values of T-1, T-2 and D-1 films coated sample were 2.06×10^{15}, 8.09×10^{15} and 2.17×10^6 Ω cm^{-2}, respectively. Therefore, it was safe to

Table 1
The electrochemical parameters of samples from the polarization curves.

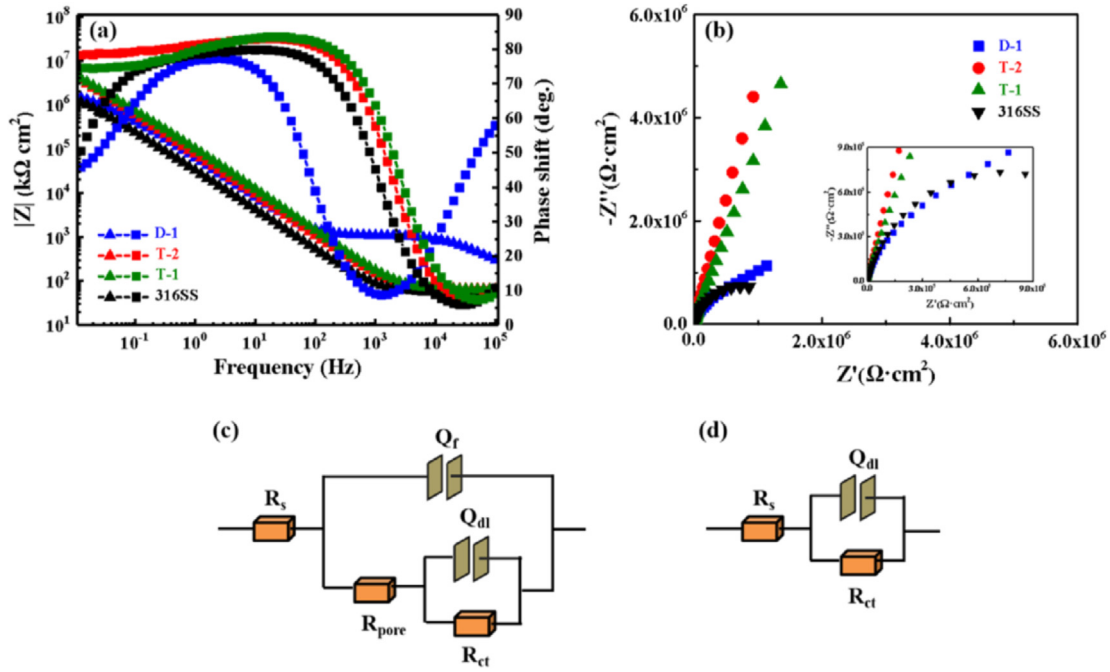| Samples	T-1	T-2	D-1	316SS
β_a (V/decade)	0.086	0.064	0.024	0.153
β_c (V/decade)	−0.021	−0.054	−0.029	−0.066
i_{corr} (A/cm^2)	2.99×10^{-10}	2.26×10^{-10}	1.53×10^{-9}	7.35×10^{-9}
E_{corr} (V, vs Ag/AgCl)	0.016	0.013	0.095	−0.200
E_{pit} (V, vs Ag/AgCl)	0.37	1.08	1.10	0.36

Fig. 7. EIS (a) Bode and (b) Nyquist plots of T-1, T-2, D-1 films coated 316SS and bare 316SS; equivalent circuits of (c) T-1, T-2, D-1 films coated 316SS, (d) bare 316SS

Table 2
Fitted parameters obtained from EIS spectra using the equivalent circuits.

	T-1	T-2	D-1	316SS
R_s (Ω cm^{-2})	23.01	34.65	40.06	53.51
Y_f (Ω^{-2} cm^{-2} S^{-n})	7.82×10^{-7}	7.16×10^{-7}	2.80×10^{-8}	–
n_f	0.67	0.72	0.88	–
R_{pore} (Ω cm^{-2})	45.13	35.17	1.02×10^3	–
Y_{dl} (Ω^{-2} cm^{-2} S^{-n})	1.31×10^{-6}	1.84×10^{-6}	3.31×10^{-6}	6.36×10^{-6}
n_{dl}	0.96	0.95	0.88	0.89
R_{ct} (Ω cm^{-2})	2.06×10^{15}	8.09×10^{15}	2.17×10^6	1.88×10^6
χ^2	3.27×10^{-4}	1.58×10^{-4}	5.61×10^{-3}	1.95×10^{-3}

conclude that T-2 film achieved the highest corrosion resistance, followed by T-1 film and D-1 film.

The excellent chemical inertness and stability of a-C film prevent its electrochemical reaction with electrolyte. However, a small amount of through porosity existed in a-C film allows for the penetration of aggressive electrolyte, triggering the occurrence of localized corrosion of the substrate. Quantitative analysis of porosity is therefore of great importance for evaluating the corrosion resistance. Standard electrochemical tests have been employed to evaluate the equivalent pore area of protective coating on an active metal substrate [32−34]. Considering the intrinsic poor conductivity and excellent chemical inertness of DLC:H and ta-C films, the electrochemical response was primarily ascribed to the substrate. Therefore, the coating porosity could be quantitatively obtained from the comparison of the electrochemical parameters measured on the bare and coated samples [35]. In this work, the electrochemical parameters deduced from the polarization curves (as shown in Table 2) were utilized to calculate the porosity (P) of the films using the empirical equation:

$$P = \frac{R_P^{L\,0}}{R_P^{L}} \times 10^{-|\Delta E_{corr}/\beta_a|} \tag{1}$$

where R_P^{L0} and R_P^{L} are the polarization resistances of the substrate and the film coated substrate, ΔE_{corr} is the potential difference

between the corrosion potential of the substrate and the film coated substrate, and β_a is the anodic Tafel slope of the substrate. The polarization resistance (R_P^{L0} and R_P^{L}) values are calculated from the Stern−Geary equation:

$$R_P = \frac{\beta_a \beta_c}{2.303 i_{corr}(\beta_a + \beta_c)} \tag{2}$$

The protective efficiency (P_i) was determined using Eq. (3):

$$P = 100(1 - \frac{i_{c0rr}}{i_{corr}^0}) \tag{3}$$

i_{corr}^0 and i_{corr} are the corrosion current density of the substrate and the film coated substrate, respectively.

The obtained porosity (P) and the protective efficiency (P_i) are showed in Fig. 8. T-1 and T-2 film presented lower porosity values
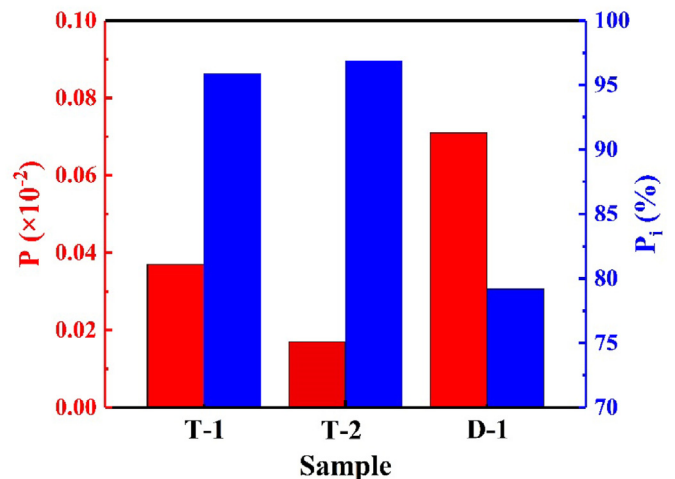

Fig. 8. The porosity (P) and protective efficiency (P_i) of T-1, T-2, D-1 film.

in comparison to D-1 film, which led to reduced exposure area of substrate to aggressive solution and thus achieved higher protective efficiency. In general, ta-C film prepared by FCVA system owns high sp^3 content and density due to the bombardment of high energy ion. The compact microstructure guaranteed good sealing effect. On the contrary, DLC:H film was of low sp^3 content and supposed to be less dense. Moreover, it was reported that hydrogen inclusion could result in porous structure [13]. Therefore, the 20 at.% hydrogen contained in DLC:H (D-1 film) network and its low sp^3 content could account for the deteriorated corrosion resistance.

The SVET was utilized to elucidate the localized corrosion processes at a microscopic level. Fig. 9 shows the SVET current density maps, in which the positive current density is related to the anodic corrosion activity of the 316SS substrate. The average anodic current densities of T-1, T-2, D-1 film coated 316SS were 1.53, 1.38, 2.15 $\mu A/cm^2$, respectively. For T-1 film coated 316SS (Fig. 9(a, d)), high current density peaks were appeared in certain areas, and a relative homogeneous distribution was observed over the scanned region. From Fig. 9 (b, e), the region with a maximum current density was diminished, revealing the attenuated electrochemical activity after thickening the ta-C film from 20 nm to 40 nm. However, several steep anode currents were emerged on the surface of D-1 film coated sample (Fig. 9(c, f)). Moreover, a rise of maximum anodic current density was detected and the area with large anode current was spread over a large area, which indicated the extended corrosion of the substrate and the poor protection ability of the DLC:H film.

4. Discussion

The electrochemical corrosion results confirmed that T-1, T-2 and D-1 film offered effective corrosion protection for 316SS in aggressive solution, and that T-2 film exhibited the best protective performance. Considering the same substrate and electrochemical test conditions, the physicochemical properties and microstructure of the a-C film could determine the electrochemical performance.

In principal, the corrosion resistance of a-C film is affected by thickness, atomic bonds and porosity [13]. The film thickness affects the physical barrier of the corrosive media. Despite the same I_D/I_G value and sp^3 contents, T-2 film significantly enhanced the pitting potential compared to that of T-1 film due to the doubled thickness. Increasing the thickness of ta-C film from 20 to 40 nm could promote the film uniformity and the effective coverage of the substrate surface, thus achieving better barrier effect. Moreover, the electron transport through the ta-C film was significantly attenuated by increasing the thickness, which helped to retard the pitting corrosion [16]. However, the DLC:H (D-1) film with thickness of 1.1 μm failed to provide effective corrosion protection, which could be attributed to atomic bonds and porosity. On the one hand, D-1 film possessed higher sp^2 content and larger sp^2 clusters in contrast to T-2 film as depicted by higher I_D/I_G value (Fig. 2) and sp^3/sp^2 ratio (Figs. 3 and 5). The enhanced graphitic phases in the amorphous carbon network resulted in increased electrical conductivity, which promoted the electron transport and accelerated the kinetics of the electrochemical reaction [16]. Moreover, a hydrogen-containing interface was more prone to corrode compared to a hydrogen-free interface, in which the H atoms was readily to lose electrons and thus hindered the formation of the passive layer [36]. Therefore, an unstable interface maybe existed between the hydrogenated D-1 film and the 316SS substrate, leading to the hazard of undermining effect. On the other hand, the porosity could play a decisive role. The lowest porosity of T-2 film was correlated to the highest protective efficiency, while the D-1 film with higher porosity presented inferior protective efficiency (Fig. 8). Moreover, the T-1 and T-2 film effectively suppressed the localized corrosion processes as compared to D-1 film (Fig. 9). The compact structure of ta-C film reduced the exposure to aggressive media and diminished the corrosion channel.

Based on above analysis, schematic diagram of corrosion mechanism for T-1, T-2, D-1 film coated 316SS is illustrated in Fig. 10. For T-1 and T-2 film, high sp^3 content ensured poor electron transportation and thus decelerated the electrochemical reaction
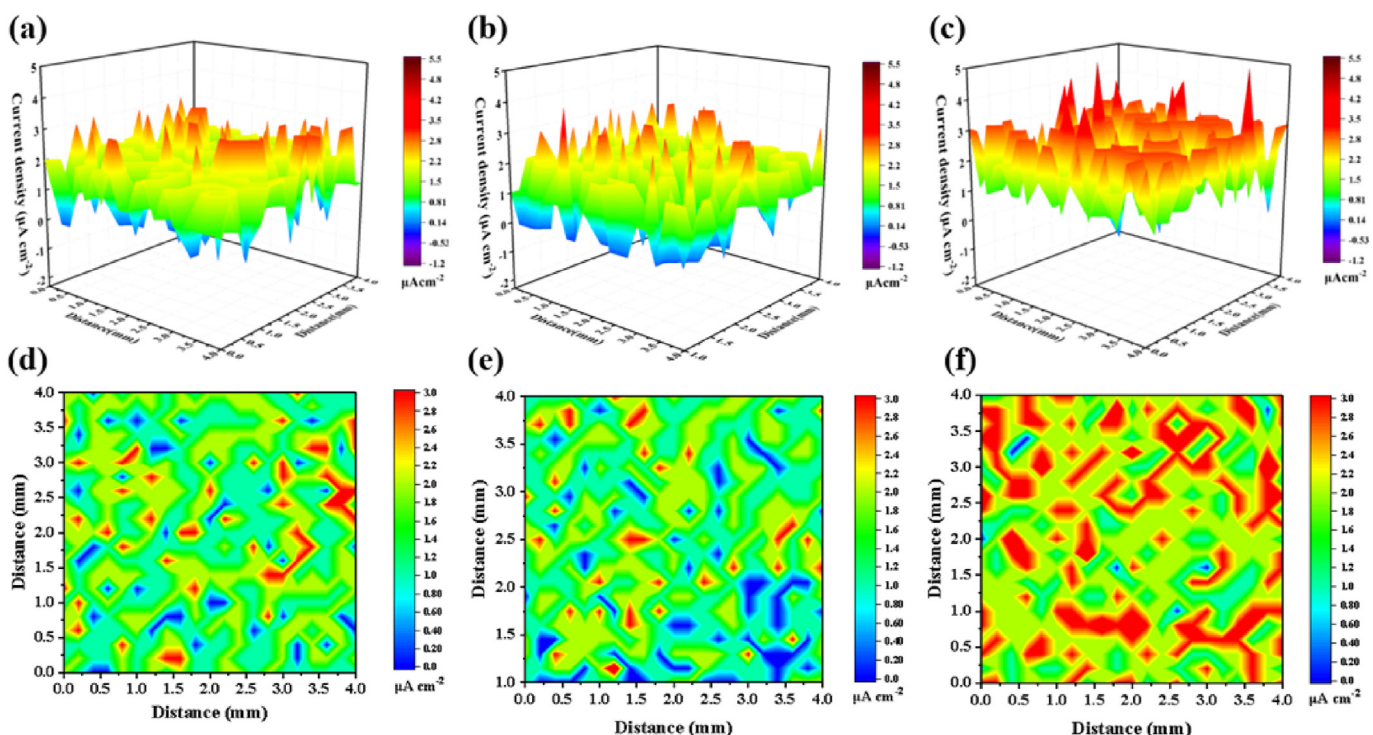

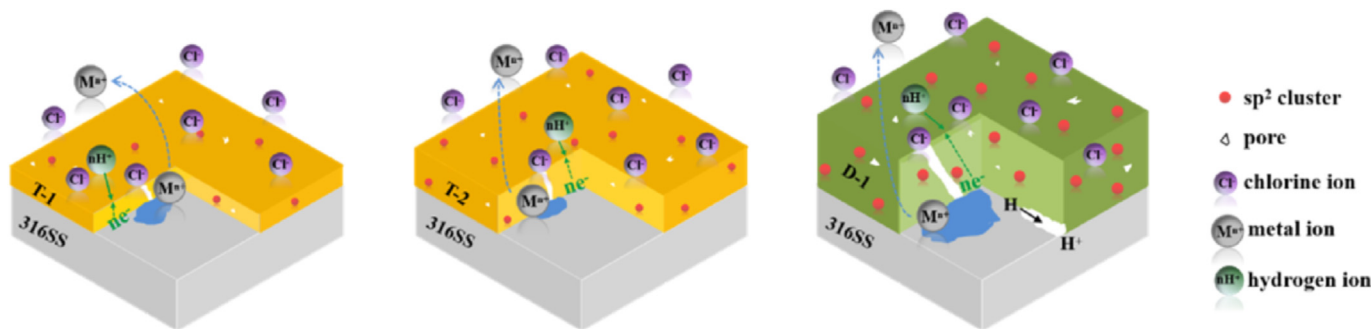**Fig. 9.** SVET current density maps of (a,d) T-1, (b,e) T-2, (c,f) D-1 film coated 316SS

Fig. 10. Schematic diagram of corrosion mechanism for T-1, T-2, D-1 film coated 316SS

occurred at the interface between film and substrate. Meanwhile, the denser structure and low porosity density of T-1 and T-2 film guaranteed the role of a good sealant for corrosion protection. In comparison to T-1 film, the thickened T-2 film enhanced the effective coverage of substrate and prolonged the diffusion channel of corrosive media, which led to improved barrier performance and delayed the occurrence of pitting corrosion. When the thick D-1 film was applied on 316SS, large amount of sp^2 clusters facilitated the charge transfer, and pore defects accelerated the permeation of electrolyte, which both led to deteriorated corrosion resistance. Meanwhile, a hydrogen-containing interface could give rise to the risk of undermining, in which hydrogen tended to lose electrons and the active substrate material captured these electrons to initiate corrosion.

The better corrosion protection achieved by 40 nm ta-C film on 316SS, as compared to 1.1 μm DLC:H film, appears highly beneficial. It is of great economic advantages to replace a thick DLC:H film with an ultra-thin ta-C film on the basis of superior electrochemical corrosion resistance, especially for the applications in the field of precise engineering components.

5. Conclusions

The corrosion behaviors of a-C films in terms of thickness, atomic bonds and porosity were investigated. Electrochemical corrosion tests were conducted on ta-C and DLC:H films prepared by FCVA and LIBD in 3.5 wt% NaCl solution. Excellent corrosion protection was achieved by 20 nm and 40 nm ta-C film, as evidenced by an order of magnitude lower corrosion current density and notable enhanced polarization resistance compared to bare substrate. The SVET revealed that ta-C film effectively suppressed the electrochemical activity of substrate. The high sealing efficiency of ta-C film was attributed to high sp^3 content and low porosity density. LSV data indicated that a certain critical thickness of ta-C film was needed to prevent the occurrence of pitting. Moreover, it could be noted that the thick DLC:H film exhibited limited corrosion protective efficiency. The large amount and size of sp^2 clusters in the carbon network of DLC:H film accelerated the kinetics of electrochemical reaction, and hydrogen inclusion or deposition induced pore defects deteriorated the sealing effects, which both led to the non-ideal corrosion behaviors of thick DLC:H film.

Declaration of competing interest

We have no conflicts of interest to this work.

CRediT authorship contribution statement

Jing Wei: Conceptualization, Methodology, Data curation, Software, Writing - original draft, Writing - review & editing. **Peng Guo:** Conceptualization, Writing - review & editing. **Linlin Liu:** Writing - review & editing. **Hanchao Li:** Data curation, Software. **Hao Li:** Data curation, Software. **Shuyuan Wang:** Data curation. **Peiling Ke:** Conceptualization, Methodology, Supervision. **Hidetoshi Saito:** Conceptualization, Methodology. **Aiying Wang:** Conceptualization, Methodology, Writing - review & editing, Supervision, Funding acquisition.

References

[1] S. Takabayashi, H. Hayashi, Y. Meng, R. Sugimoto, S. Ogawa, Y. Takakuwa, Chemical structure and electrical characteristics of diamondlike carbon films, Diam. Relat. Mater. 81 (2018) 16–26, https://doi.org/10.1016/j.diamond.2017.11.005.

[2] X. Han, J. Zhu, J. Han, M. Tan, Z. Jia, C. Jiang, Stress, mechanical and adhesion properties of multilayer tetrahedral amorphous carbon films, Appl. Surf. Sci. 255 (2008) 607–609, https://doi.org/10.1016/j.apsusc.2008.06.087.

[3] K. Bewilogua, D. Hofmann, History of diamond-like carbon films — from first experiments to worldwide applications, Surf. Coating. Technol. 242 (2014) 214–225, https://doi.org/10.1016/j.surfcoat.2014.01.031.

[4] T.F. Zhang, Q.Y. Deng, B. Liu, B.J. Wu, F.J. Jing, Y.X. Leng, N. Huang, Wear and corrosion properties of diamond like carbon (DLC) coating on stainless steel, CoCrMo and Ti6Al4V substrates, Surf. Coating. Technol. 273 (2015) 12–19, https://doi.org/10.1016/j.surfcoat.2015.03.031.

[5] AZZI, AMIRAULT, PAQUETTE, KLEMBERGSAPIEHA, E. J., MARTINU, Corrosion performance and mechanical stability of 316L/DLC coating system: role of interlayers, Surf. Coating. Technol. 204 (2010) 3986–3994, https://doi.org/10.1016/j.surfcoat.2010.05.004.

[6] Z.M. Wang, J. Zhang, X. Han, Q.F. Li, Z.L. Wang, R. Wei, Corrosion and salt scale resistance of multilayered diamond-like carbon film in CO_2 saturated solutions, Corrosion Sci. 86 (2014) 261–267, https://doi.org/10.1016/j.corsci.2014.05.015.

[7] R.J. Waltman, J. Joseph, X.C. Guo, An AFM Study of corrosion on rigid magnetic disks, Corrosion Sci. 52 (2010) 1258–1262, https://doi.org/10.1016/j.corsci.2010.01.004.

[8] T.M. Manhabosco, L.A.M. Martins, S.M. Tamborim, M. Ilha, M.Q. Vieira, F.C.R. Guma, I.L. Müller, Cell response and corrosion behavior of electrodeposited diamond-like carbon films on nanostructured titanium, Corrosion Sci. 66 (2013) 169–176, https://doi.org/10.1016/j.corsci.2012.09.015.

[9] R.A. Bernal, P. Chen, J.D. Schall, J.A. Harrison, Y.-R. Jeng, R.W. Carpick, Influence of chemical bonding on the variability of diamond-like carbon nanoscale adhesion, Carbon 128 (2018) 267–276, https://doi.org/10.1016/j.carbon.2017.11.040.

[10] O.V. Penkov, M. Khadem, J.S. Lee, M. Kheradmandfard, C.L. Kim, S.W. Cho, D.E. Kim, Highly durable and biocompatible periodical Si/DLC nanocomposite coatings, Nanoscale 10 (2018) 4852–4860, https://doi.org/10.1039/

c7nr06762c.

[11] Z.A. Boeva, A. Catena, L. Höfler, S. Wehner, C.B. Fischer, T. Lindfors, Improved water barrier properties of polylactic acid films with an amorphous hydrogenated carbon (a-C:H) coating, Carbon 120 (2017) 157–164, https://doi.org/10.1016/j.carbon.2017.05.005.

[12] N.W. Khun, E. Liu, X.T. Zeng, Corrosion behavior of nitrogen doped diamond-like carbon thin films in NaCl solutions, Corrosion Sci. 51 (2009) 2158–2164, https://doi.org/10.1016/j.corsci.2009.05.050.

[13] A.S. Hamdy, Electrochemical behavior of diamond-like-carbon coatings deposited on AlTiC (AlO + TiC) ceramic composite substrate in HCl solution, Electrochim. Acta 56 (2011) 1554–1562, https://doi.org/10.1016/j.electacta.2010.11.021.

[14] Y. Uematsu, K. Tokaji, H. Takekawa, Effect of thick DLC coating on fatigue behaviour of magnesium alloy in laboratory air and demineralised water, Fatig. Fract. Eng. Mater. Struct. 33 (2010) 607–616, https://doi.org/10.1111/j.1460-2695.2010.01470.x.

[15] S. Sainio, D. Nordlund, M.A. Caro, R. Gandhiraman, J. Koehne, N. Wester, J. Koskinen, M. Meyyappan, T. Laurila, Correlation between sp3-to-sp2 ratio and surface oxygen functionalities in tetrahedral amorphous carbon (ta-C) thin film electrodes and implications of their electrochemical properties, J. Phys. Chem. C 120 (2016), https://doi.org/10.1021/acs.jpcc.6b02342.

[16] T. Palomäki, N. Wester, M.A. Caro, S. Sainio, V. Protopopova, J. Koskinen, T. Laurila, Electron transport determines the electrochemical properties of tetrahedral amorphous carbon (ta-C) thin films, Electrochim. Acta 225 (2017) 1–10, https://doi.org/10.1016/j.electacta.2016.12.099.

[17] L. Joska, J. Fojt, The effect of porosity on barrier properties of DLC layers for dental implants, Appl. Surf. Sci. 262 (2012) 234–239, https://doi.org/10.1016/j.apsusc.2012.07.013.

[18] A. Zeng, E. Liu, I.F. Annergren, S.N. Tan, S. Zhang, P. Hing, J. Gao, EIS capacitance diagnosis of nanoporosity effect on the corrosion protection of DLC films, Diam. Relat. Mater. 11 (2002) 160–168, https://doi.org/10.1016/S0925-9635(01)00568-4.

[19] N. Konkhunthot, P. Photongkam, P. Wongpanya, Improvement of thermal stability, adhesion strength and corrosion performance of diamond-like carbon films with titanium doping, Appl. Surf. Sci. 469 (2019) 471–486, https://doi.org/10.1016/j.apsusc.2018.11.028.

[20] L. Mohan, C. Anandan, V.K.W. Grips, Corrosion behavior of titanium alloy Beta-21S coated with diamond like carbon in Hank's solution, Appl. Surf. Sci. 258 (2012) 6331–6340, https://doi.org/10.1016/j.apsusc.2012.03.032.

[21] Y. Wu, S. Zhou, W. Zhao, O. Lu, Comparative corrosion resistance properties between (Cu, Ce)-DLC and Ti co-doped (Cu, Ce)/Ti-DLC films prepared via magnetron sputtering method, Chem. Phys. Lett. 705 (2018) 50–58, https://doi.org/10.1016/j.cplett.2018.05.061.

[22] G.F. Huang, L. Zhou, W. Huang, L. Zhao, S. Li, D. Li, The mechanical performance and anti-corrosion behavior of diamond-like carbon film, Diam. Relat. Mater. 12 (2003) 1406–1410, https://doi.org/10.1016/S0925-9635(03)00168-7.

[23] M. Zhong, C. Zhang, J. Luo, The protective properties of ultra-thin diamond-like carbon films for high density magnetic storage devices, Appl. Surf. Sci. 256 (2009) 322–328, https://doi.org/10.1016/j.apsusc.2009.08.023.

[24] M. Tan, Y. Yan, H. Zhang, X. Han, J. Zhu, J. Han, H. Ma, Corrosion protection of ultra-thin ta-C films for recording slider applications at varied substrate bias, Surf. Coating. Technol. 203 (2009) 963–966, https://doi.org/10.1016/j.surfcoat.2008.08.077.

[25] J. Wei, H. Li, L. Liu, P. Guo, P. Ke, A. Wang, Enhanced tribological and corrosion properties of multilayer ta-C films via alternating sp3 content, Surf. Coating. Technol. 374 (2019) 317–326, https://doi.org/10.1016/j.surfcoat.2019.05.087.

[26] C. Kong, P. Guo, L. Sun, Y. Zhou, Y. Liang, X. Li, P. Ke, K.-R. Lee, A. Wang, Tribological mechanism of diamond-like carbon films induced by Ti/Al co-doping, Surf. Coating. Technol. 342 (2018) 167–177, https://doi.org/10.1016/j.surfcoat.2018.02.098.

[27] P. Guo, R. Chen, L. Sun, X. Li, P. Ke, Q. Xue, A. Wang, Bulk-limited electrical behaviors in metal/hydrogenated diamond-like carbon/metal devices, Appl. Phys. Lett. 112 (2018) 33502, https://doi.org/10.1063/1.5003297.

[28] A.C. Ferrari, J. Robertson, Resonant Raman spectroscopy of disordered, amorphous, and diamondlike carbon, Phys. Rev. B Condens. Matter 64 (2001) 75414, https://doi.org/10.1103/PhysRevB.64.075414.

[29] B. Lesiak, L. Kövér, J. Tóth, J. Zemek, P. Jiricek, A. Kromka, N. Rangam, C sp^2/sp^3 hybridisations in carbon nanomaterials — XPS and (X)AES study, Appl. Surf. Sci. 452 (2018) 223–231, https://doi.org/10.1016/j.apsusc.2018.04.269.

[30] S. Singh, N. Verma, Fabrication of Ni nanoparticles-dispersed carbon micro-nanofibers as the electrodes of a microbial fuel cell for bio-energy production, Int. J. Hydrogen Energy 40 (2015) 1145–1153, https://doi.org/10.1016/j.ijhydene.2014.11.073.

[31] S. Singh, N. Verma, Graphitic carbon micronanofibers asymmetrically dispersed with alumina-nickel nanoparticles: a novel electrode for mediatorless microbial fuel cells, Int. J. Hydrogen Energy 40 (2015) 5928–5938, https://doi.org/10.1016/j.ijhydene.2015.03.010.

[32] V. de Freitas Cunha Lins, G.F. de Andrade Reis, C.R. de Araujo, T. Matencio, Electrochemical impedance spectroscopy and linear polarization applied to evaluation of porosity of phosphate conversion coatings on electrogalvanized steels, Appl. Surf. Sci. 253 (2006) 2875–2884, https://doi.org/10.1016/j.apsusc.2006.06.030.

[33] D.A. Shores, Corrosion and metal release rates of Ni substrates under a porous gold coating, Corrosion Sci. 50 (2008) 372–383, https://doi.org/10.1016/j.corsci.2007.08.010.

[34] J. Creus, H. Mazille, H. Idrissi, Porosity evaluation of protective coatings onto steel, through electrochemical techniques, Surf. Coating. Technol. 130 (2000) 224–232, https://doi.org/10.1016/s0257-8972(99)00659-3.

[35] S. Mirhashemihaghighi, J. Światowska, V. Maurice, A. Seyeux, S. Zanna, E. Salmi, M. Ritala, P. Marcus, Corrosion protection of aluminium by ultra-thin atomic layer deposited alumina coatings, Corrosion Sci. 106 (2016) 16–24, https://doi.org/10.1016/j.corsci.2016.01.021.

[36] T.F. Zhang, B.J. Wu, Q.Y. Deng, W.J. Huang, N. Huang, Y.X. Leng, Effect of a hydrogenated interface on the wear behavior of a diamond-like carbon film in a water environment, Diam. Relat. Mater. 74 (2017) 53–58, https://doi.org/10.1016/j.diamond.2017.02.007.